Broadband low-frequency sound attenuation in duct with embedded periodic sonic black holes

Yongzhen Mi [a], Li Cheng [b], Wei Zhai [c], Xiang Yu [a,b,*]

[a] *Institute of High Performance Computing, ASTAR, 138632, Singapore*
[b] *Department of Mechanical Engineering, The Hong Kong Polytechnic University, 999077, Hong Kong*
[c] *Department of Mechanical Engineering, National University of Singapore, 117411, Singapore*

ABSTRACT

This paper studies the sound wave propagation and attenuation characteristics in a new type of acoustic device, which is constructed by periodically embedding sonic black holes (SBHs) into an air-filled waveguide. The SBH is realized by cascading a set of rigid rings with linearly or quadratically changing inner radii into each unit cell section. Acoustic impedance variation rendered by this specially tailored profile progressively slows down the incident sound velocity to generate the SBH effects including wavelength compression, energy focalization, and dissipation with inherent damping in the duct. Upon developing and validating a model based on the transfer matrix method (TMM), the sound transmission loss (STL) of a finite-length periodic duct with different geometrical parameters is investigated. Different from a single SBH unit which can trigger the complete SBH process only above the cut-on frequency, the proposed periodic arrangement offers strong attenuation bands in the low-frequency range of the STL curve well below the frequency barrier imposed by the cut-on frequency of a single SBH unit. Mechanism studies reveal that these attenuation bands result from the interplay between the Bragg scattering and the SBH-specific slow-sound effects. The latter is shown to equivalently increase the effective lattice constant of the periodic duct, thus lowering the frequency of the Bragg bandgap. It is also shown that in contrast to conventional locally-resonant metamaterials, the proposed device exhibits far less dependence on the number of unit cells and the amount of rigid rings to activate a significant low-frequency stop-band. These appealing features could greatly simplify the design and application of SBH-based metamaterials, making it a promising solution for low-frequency wave manipulation and noise control.

1. Introduction

Acoustic black hole (ABH) arouses great research interest in recent years. It is typically achieved by continuously varying the acoustic impedance in the direction of wave propagation in a waveguide, such that the wave speed is progressively reduced and ideally a non-reflecting condition is realized [1–3]. To activate the ABH effect, the characteristic impedance of the ABH termination should equal to that of the waveguide at their interface. The phase velocity of incoming waves gradually slows down as it travels closer to the end. As the local admittance at the end goes to infinity in the theoretical limit, the wave velocity can be reduced completely to zero,

* Corresponding author.
  E-mail address: yuxiang@ihpc.a-star.edu.sg (X. Yu).

implying that the incoming propagating waves will never reach the end. Such a phenomenon can, in principle, be created for certain types of waves in either solids [1] or fluids [4,5]. Most existing ABH studies focus on flexural wave propagation in structures, such as beams, plates, solids, etc. For sound waves in air, the term "sonic black hole (SBH)" was coined by Mironov and Pislyakov [6] to differentiate from its structural counterpart – vibrational black hole (VBH). Both fall into the category of acoustic black hole (ABH).

The ABH theory for structural wave propagation has been extensively studied by far [7–9]. The required variation of the local admittance in a structural ABH is commonly realized by tailoring the thickness of a thin-walled structure to follow a power-lawed profile [10]. This usually results in a taper [11,12], a wedge [13,14], or an indentation [15–17] onto a plate structure, in which elastic waves propagate with decaying phase velocity. ABH phenomenon can be exploited to achieve enhanced passive vibration isolation. For example, Tang et al. [18] investigated the low-frequency transmission attenuation bands in a composite beam embedded with double-leaf acoustic black hole indentations. Experimental results show that strong vibration attenuation could be generated using as few as three ABH elements. Zhou et al. [19] proposed a planar swirl-shaped design of the ABH-based vibration absorber, in which the bending-twisting coupling effect produces wave retardings in both transverse and torsional movements. An alternative design was proposed by Li et al. [20] which combines the ABH with nonlinear vibration absorbers to obtain broadband vibration mitigation. A major shortcoming of the structural ABH is that its theoretical implementation heavily relies on perfectly diminishing the power-law profile to zero. Even a small residual thickness at the end can incur unavoidable wave reflections and eventually jeopardize the expected ABH effects. In practical implementation, this shortcoming can be mitigated by adding damping treatment to the ABH, such as attaching a thin layer of viscoelastic material to the surface of the beam or the plate [21]. Particularly, owing to the wave amplitude increase and the vibrational energy concentration, deploying damping treatment over a small area near the tip would be able to provide the required dissipation [22]. A comprehensive summary of the state-of-the-art ABH technologies can be found in the recent review paper [23].

Comparatively, SBH effects for sound waves in air are less exploited. The first occurrence of the SBH was proposed by Mironov et al. [2], in which the reduction of sound velocity was discretely achieved by inserting a set of rigid rings into a retarding duct with decaying inner radii. The effects of main design parameters on the reflection coefficient were further studied in [24]. Guasch et al. [25] investigated the SBH phenomenon by modeling the SBH as a meta-fluid with a power-law varying density. The theoretical formulation of the SBH effect was also discussed by Hollkamp et al. in [26]. As an alternative, Mironov et al. [6] proposed a different SBH design, in which the rigid rings were replaced by rigid discs with increasing diameters fixed on four rods. In our recent publication [27], we explored the wave trapping mechanism from both sound transmission and absorption perspectives. It was found that an open-end ABH can simultaneously reduce sound reflection and transmission. The SBH could also be combined with classical devices to create hybrid acoustic absorbers, such as the recent work on SBH-backed micro-perforated plates [28].

Despite these efforts, two major problems remain to be tackled for practical applications of SBH-based technology. The first one is associated with the cut-on frequency [2], only above which the desired ABH effect, in terms of wave-speed-induced energy focusing and dissipation, becomes systematic when the incoming sound wavelength starts to match the physical SBH dimension. This means that moving the cut-on frequency downwards to lower frequencies would require a very bulky structure. The second problem is tied with the practical implementation of the SBH. Previous results show that for a single SBH termination, a large number of rigid rings are necessary to ensure a fast and smooth reduction of the reflection coefficient as frequency increases [24]. However, from the viewpoint of manufacturing, squeezing a large number of rigid rings into a narrow duct is challenging and problematic.

To tackle the aforementioned problems, the present study employs SBH as building blocks to construct a periodic duct, instead of as a single retarding termination, to study the potential benefits arising from the design for acoustic wave manipulation and sound attenuation. A similar idea was exploited for structural ABH by Tang et al. [29] to achieve vibration reduction of a flexural beam. It was shown that the vibration of the beam was significantly suppressed with only a few embedded ABH cells. Following the same philosophy, this paper is motivated with two hypotheses: first, as periodicity could trigger the Bragg scattering effect, the low-frequency bandgaps, typically existing in periodic structures, could possibly overcome the hurdle imposed by the cut-on frequency of a single SBH [30–32]. Second, with more unit cells, the strict requirement on the number of inner rings for each unit cell could possibly be reduced [33]. The proposed device is also expected to overcome the limitations of traditional acoustic metamaterials formed by periodic Helmholtz resonators [34–37], which typically exhibit narrow local-resonance bandgaps [38], or heavy reliance on the periodicity [39].

The physics associated with the way that SBH effect plays out in the proposed periodic configuration also need a deeper understanding. It is well-known that effective sound absorption in a single SBH unit relies on two mechanisms working simultaneously, i.e., energy concentration due to the slowing-down of the sound speed and adequate energy dissipation [27]. These two conditions can only be satisfied at relatively high frequencies, such that the low frequency performance of a single SBH is usually weak. The rationale behind the proposed periodic SBH construction is to boost the low-frequency sound attenuation by capitalizing on the Bragg scattering effect in the retarding structure rather than purely relying on dissipation. In fact, as the speed of sound that travels through each SBH unit is determined by its profile of changing inner radii, the slow-sound effect would still preserve at low frequencies, thus partially activating the SBH process despite the absence of energy dissipation. This alludes to the possibility of triggering the formation of bandgaps linked to Bragg reflections at lower frequencies than the ones usually determined by the lattice constant of the conventional periodic structure, as the sound speed is equivalently reduced. This motivates us to find out how such sound speed variation would benefit the formation of the Bragg bandgaps in views of noise mitigation.

In the following, we will thoroughly examine these possibilities and the underlying mechanisms by means of numerical simulation and experiments. This study provides both the theoretical background and design guidelines for conceiving an acoustic device made of periodic SBHs. The study intends to show the potential offered by the SBH-based design for acoustic wave manipulation and low-frequency and broadband noise control.

2. Theoretical model and formulation

2.1. Model description of the proposed device

The proposed acoustic duct with embedded periodic SBHs is illustrated in Fig. 1. Each element in the periodic duct is called a unit cell, which comprises a segment with varying cross-sections sandwiched by two uniform parts. As shown in the inset of Fig. 1(a), the proposed SBH features a symmetric arrangement of shirking and expanding rings. The profile is symmetrical with respect to the midpoint. This differs from the classical SBH design, which usually acts as a termination to a regular duct and only has a shrinking inner cavity. The inner radius of rings in the two parts take either a linear variation (Fig. 1b)

$$y = \frac{R - r}{b}|x| + r \tag{1}$$

or a quadratic variation (Fig. 1c)

$$y = \frac{R - r}{b^2}x^2 + r \tag{2}$$

where R is the radius of the uniform cross-section; r is the radius at the thinnest cross-section, or the residual radius; b is the axial length of the shrinking half or the expanding half. Note that $y(\pm b) = R$ and $y(0) = r$ for both configurations. Each uniform part also has an axial length of b, so the total length of one unit cell, referred to as the lattice constant a, is $4b$. In this paper, we only focus on these two types of SBHs with low power-law exponents, as evidence shows that power-lawed profiles with higher exponents would violate the smoothness criteria and thus impair the SBH effect [23].

The purpose of such a symmetrical SBH profile is to strike a balance between the sound-dissipating nature of each single SBH and the creation of Bragg bandgaps arising from the periodic arrangement. With symmetrical SBH profiles, the upstream unit cells permit a portion of the incident sound waves to propagate downwards and be reflected by those downstream unit cells. Interactions between the incident and reflected sound waves give rise to Bragg bandgaps, which would not occur if most sound waves have already been dissipated by the first unit cell with an otherwise more perfect SBH profile. The right half of the symmetrical SBH reverses the transformation process that the sound waves have undergone in the left half, enabling the expected downward propagation. Such a design cannot be achieved if the right half is missing, since an abrupt change of cross-section at the end of the left half will only result in more sound reflections.

2.2. Formulation by the transfer matrix method

For a perfect SBH termination with its inner radii of the rings decaying to zero, the governing equations of the in-duct acoustic propagation and their solutions have been detailed in [24]. However, due to the presence of the residual radius, it is rather difficult to
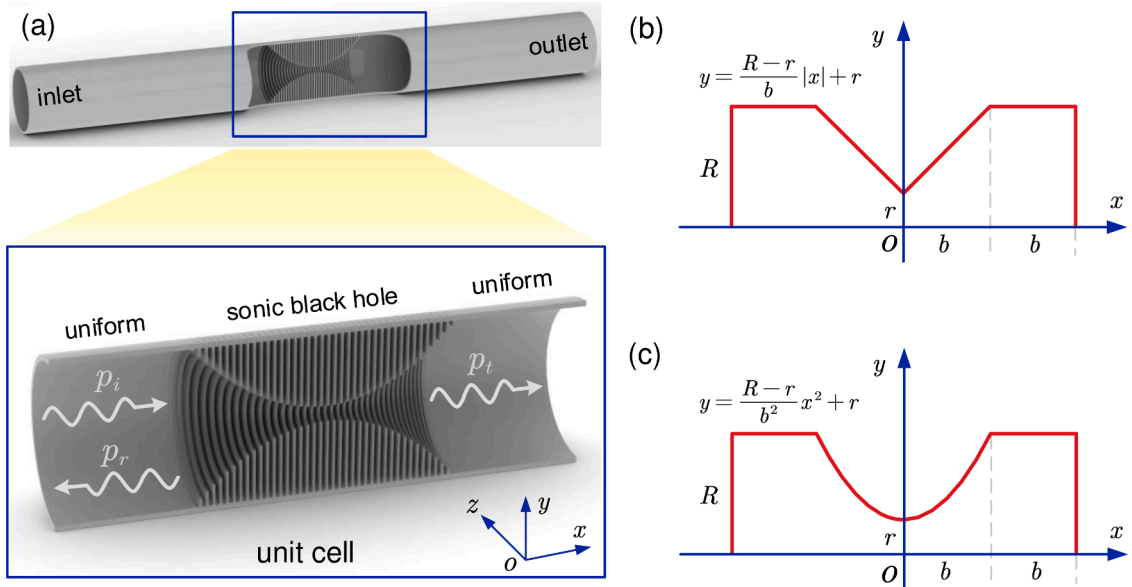
Fig. 1. Schematic of the sonic black hole: (a) an acoustic duct with embedded SBHs and a cutaway view of its unit cell. Each unit cell consists of a symmetrically power-lawed section sandwiched by two identical uniform sections; (b) axial profile of one SBH unit cell with linearly changing radii; (c) axial profile of one SBH unit cell with quadratically changing radii. The formulas for the power-lawed profiles are given along the figures.

apply these prior equations to the current design. Next, we follow the method proposed by [24] and seek a solution based on the transfer matrix method (TMM). With the TMM, state vectors (sound pressure p and volume velocity u) at two arbitrary sections of the duct can be linked up by an analytical transfer matrix under the plane wave framework. In the proposed device, the rigid rings in each unit cell are assumed to have the same thickness and placed at equal intervals. The acoustic duct is filled by air, which is characterized by the sound speed c_0 and mass density ρ_0.

A segment of the SBH portion is depicted in Fig. 2(a), which consists of two successive rigid rings and the duct wall in between. For ease of modeling, the acoustic cavity enclosed by this ring-wall-ring segment is divided into four parts: a pair of cylindrical cavities inside the two rings, a conical cavity bridging the two cylindrical cavities, and a branch cavity appended to the conical cavity. The four cavities are illustrated in Fig. 2(b), and four coordinates, x_{i+2}, x_{i+1}, x_i, and x_{i-1}, are labelled on the x-axis to indicate their locations. The inner radii of the left and right rings are represented by r_{i+1} and r_i, respectively.

First, the state vector at x_{i+2}, $(p_{i+2} \quad u_{i+2})^{\mathrm{T}}$, is related to the state vector at x_{i+1}, $(p_{i+1} \quad u_{i+1})^{\mathrm{T}}$ as

$$\begin{Bmatrix} p_{i+2} \\ u_{i+2} \end{Bmatrix} = \mathbf{T}_1^i \begin{Bmatrix} p_{i+1} \\ u_{i+1} \end{Bmatrix} \tag{3}$$

2.3. The transfer matrix $\mathbf{T}_1^i$ in eq. (3) is expressed as

$$\mathbf{T}_1^i = \begin{bmatrix} \cos(k_0 h_r) & j\dfrac{Z_0}{S_{i+1}}\sin(k_0 h_r) \\ j\dfrac{S_{i+1}}{Z_0}\sin(k_0 h_r) & \cos(k_0 h_r) \end{bmatrix} \tag{4}$$

where j is the imaginary unit; $k_0 = \omega/c_0$ is acoustic wavenumber and ω is the angular frequency; $Z_0 = \rho_0 c_0$ denotes the characteristic impedance; $h_r = x_{i+1} - x_{i+2}$ is the ring thickness and $S_{i+1} = \pi r_{i+1}^2$ is the cross-sectional area of the duct at x_{i+1}.

Then, the state vector at x_{i+1}, $(p_{i+1} \quad u_{i+1})^{\mathrm{T}}$ is forwarded to the state vector at x_i, $(p_i \quad u_i)^{\mathrm{T}}$ as

$$\begin{Bmatrix} p_{i+1} \\ u_{i+1} \end{Bmatrix} = \mathbf{T}_2^i \mathbf{T}_3^i \begin{Bmatrix} p_i \\ u_i \end{Bmatrix} \tag{5}$$

where $\mathbf{T}_2^i$ is obtained by simply replacing h_r in Eq. (4) with h_i and $h_i = x_i - x_{i+1}$ stands for the width of the conical cavity. Since volume velocities are used in the state vectors instead of particle velocities, the difference in the cross-sectional areas at the entrance and exit of the conical cavity is automatically incorporated. $\mathbf{T}_3^i$ is the transfer matrix that characterizes the branch cavity, which is written as

$$\mathbf{T}_3^i = \begin{bmatrix} 1 & 0 \\ Y_3 & 1 \end{bmatrix} \tag{6}$$

2.4. The Y_3 in eq. (6) is the admittance of the branch cavity

$$Y_3 = j\frac{k_0}{Z_0}V_3 \tag{7}$$

in which V_3 is the volume of the branch cavity

$$V_3 = \pi h_i \left[R^2 - \frac{r_i^2 + r_{i+1}^2 + r_i r_{i+1}}{3} \right] \tag{8}$$
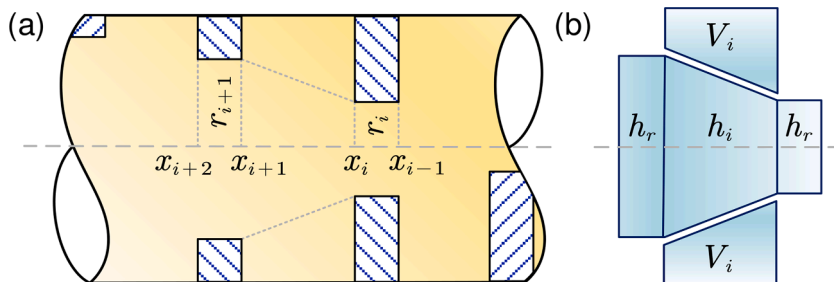
Fig. 2. Schematic of the transfer matrix method: (a) a ring-wall-ring segment in the SBH portion of the acoustic duct; (b) the acoustic cavities enclosed by the ring-wall-ring segment.

2.5. Substituting eq. (5) into eq. (3) yields the transfer matrix relation for the ring-wall-ring segment

$$\begin{Bmatrix} p_{i+2} \\ u_{i+2} \end{Bmatrix} = \mathbf{T}_1^i \mathbf{T}_2^i \mathbf{T}_3^i \begin{Bmatrix} p_i \\ u_i \end{Bmatrix} = \mathbf{T}^i \begin{Bmatrix} p_i \\ u_i \end{Bmatrix} \tag{9}$$

2.6. Solutions for infinite and finite configurations

Repeating the deviation of Eq. (9) for the remaining ring-wall-ring segments, the transfer matrix of the entire SBH portion in one unit cell is obtained as a successive product of all segmental transfer matrices

$$\mathbf{T}^{\mathrm{SBH}} = \prod_{i=1}^{N} \mathbf{T}^i \tag{10}$$

where N is the total number of ring-wall-ring segments in the SBH portion.

2.7. The transfer matrix of one unit cell is thus written as

$$\mathbf{T}^{\mathrm{UC}} = \mathbf{T}^0 \mathbf{T}^{\mathrm{SBH}} \mathbf{T}^0 \tag{11}$$

where $\mathbf{T}^0$ is the transfer matrix of the uniform portion, which is again obtained by replacing h_r and S_{i+1} in Eq. (4) by b and $S_0 = \pi R^2$, respectively.

Based on Eq. (11), various metrics characterizing the wave propagation properties and sound attenuation performance inside the duct can be steadily obtained. For an infinite configuration (Fig. 3a), the two sets of state vectors at the beginning and the end of the n-th unit cell can be related based on the Bloch's theorem [7]:

$$\begin{Bmatrix} p_{n+1} \\ u_{n+1} \end{Bmatrix} = e^{-jqa} \begin{Bmatrix} p_n \\ u_n \end{Bmatrix} \tag{12}$$

in which q is the wavenumber of the Bloch wave in the x direction; $a = 4b$ is the lattice constant.

2.8. Substituting eq. (11) into eq. (12) yields a standard eigenvalue problem

$$\left(\mathbf{T}^{\mathrm{UC}} - e^{-jqa} \mathbf{I} \right) \begin{Bmatrix} p_n \\ u_n \end{Bmatrix} = 0 \tag{13}$$

which provides the dispersive relation of the acoustic waves in the periodic duct through $|\mathbf{T}^{\mathrm{UC}} - e^{-jqa}\mathbf{I}| = 0$.

The solution of Eq. (13) leads to the dispersive relation of acoustic waves propagating along the periodic duct. This relation is also known as band diagram when the Bloch wavenumber q or the normalized wavenumber qa is plotted as a function of frequency. The band diagram consists of a real part and an imaginary part, representing wave propagation and attenuation in the periodic medium, respectively.
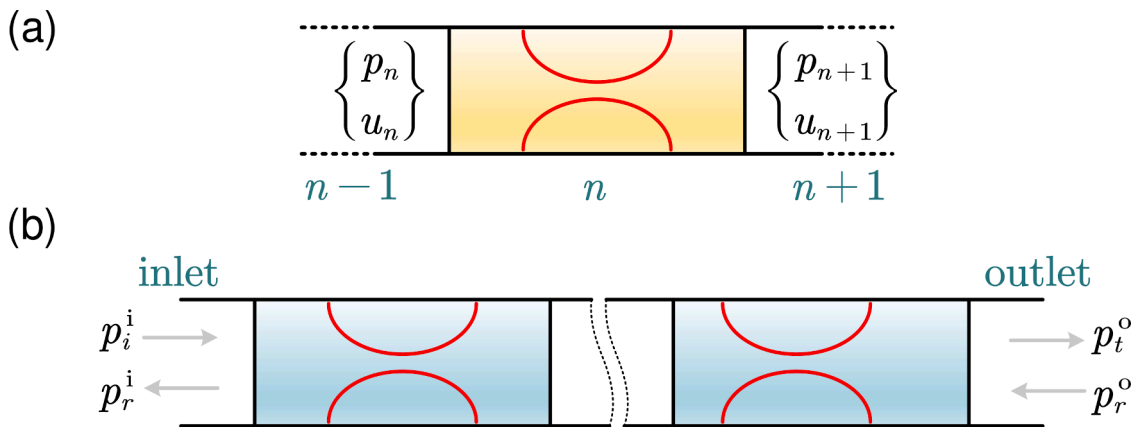
Fig. 3. Configurations of the acoustic duct for solutions of various noise reduction indicators: (a) one unit cell out of an infinite duct for bandgap calculation; (b) a finite-length duct comprising several unit-cells with an anechoic/ rigid outlet to calculate the STL.

2.9. The transfer matrix for a finite-length duct is written as a successive product of the transfer matrices contributed by all unit cells

$$\begin{Bmatrix} p_{\text{in}} \\ u_{\text{in}} \end{Bmatrix} = \left(\mathbf{T}^{\text{UC}}\right)^n \begin{Bmatrix} p_{\text{out}} \\ u_{\text{out}} \end{Bmatrix} = \mathbf{T} \begin{Bmatrix} p_{\text{out}} \\ u_{\text{out}} \end{Bmatrix} \tag{14}$$

where n is the total number of unit cells.

For different applications, a finite-length duct may have an open or closed outlet. The Sound Transmission Loss (STL) is commonly employed to quantify the noise insulation performance of an open-end duct, which is calculated from the elements of the transfer matrix $\mathbf{T}$ [34]:

$$\text{STL} = 20\log_{10}\left|\frac{1}{2}\left(\mathbf{T}(1,1) + \mathbf{T}(1,2)\frac{S_0}{Z_0} + \mathbf{T}(2,1)\frac{Z_0}{S_0} + \mathbf{T}(2,2)\right)\right| \tag{15}$$

3. Numerical results and discussions

In this section, the physical mechanisms of the periodic SBHs and the influences of several key geometrical parameters will be studied. These parameters include the number of rings in the SBH portion of one unit cell N, the number of unit cells in a finite-length acoustic duct n, the thickness of each rigid ring h_r, and the residual radius r. We will investigate the physical mechanisms underpinning the acoustic wave propagation and attenuation in the duct, in particular when N or n is smaller than what is typically demanded in traditional SBH and acoustic meta-material settings. With insights gained, numerical studies will be carried out to demonstrate the advantages of the proposed device.

The inner radius and axial length of the uniform portion are fixed at $R = 0.03$m and $b = 0.05$m, which are selected to be compatible with the dimensions of the impedance tube used for the subsequent experimental STL measurement. The cut-off frequency of the acoustic duct with $R = 0.03$m is $f_c = 1.84c_0/(2\pi R) = 3300$Hz. In the numerical simulation, the maximum frequency range is capped at 1500 Hz to ensure the validity of the plane wave assumption used in the TMM calculation.

3.1. Mechanism studies

3.1.1. Baseline model results and validation

To get a basic understanding of the acoustic duct, we first calculate the STLs of two baseline models equipped with periodic linear and quadratic SBHs, respectively. The baseline models are finite-length ducts with the same geometrical parameters: $N = 20$, $n = 3$, $h_r : h_i = 1 : 3$, and $r = R/10$. The air domain is first assumed as lossless. The STL curves are shown in Fig. 4, where the FEM results obtained from COMSOL Multiphysics simulations are also added for comparison. The FEM models are meshed using tetrahedral elements with an average size of 2 mm, which is adequate to serve as sufficiently accurate references. To calculate the STL using COMSOL, a background plane wave is applied at the entrance of the duct and the radiated sound power is evaluated at the downstream with a non-reflecting boundary definition. Then, the STL is calculated using Eq. (15). From Fig. 4, an excellent agreement between the
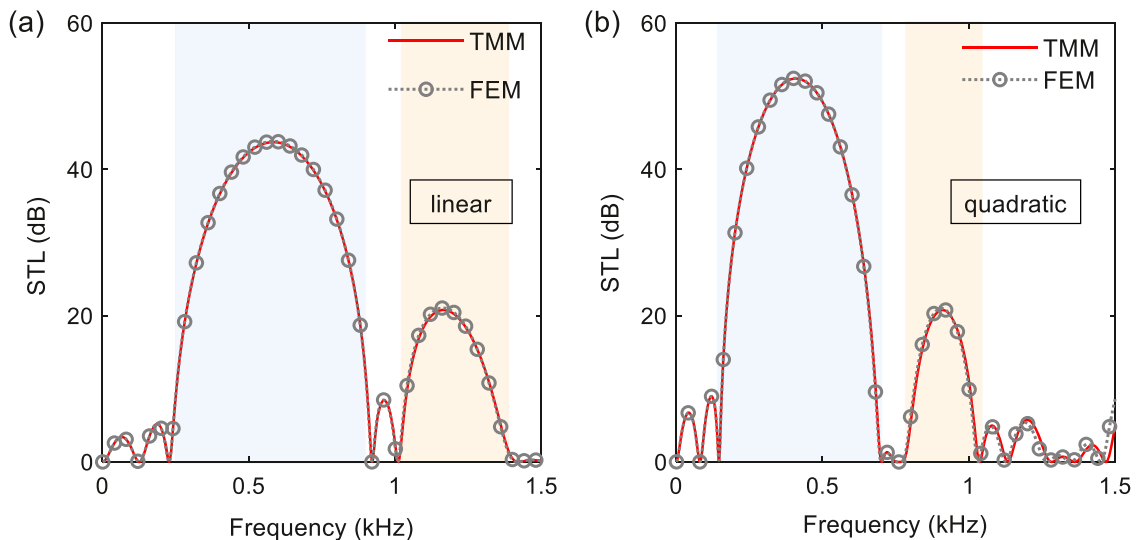
Fig. 4. STLs of the acoustic duct with its SBH portion following a (a) linear; (b) quadratic inner radius variations. Other geometrical parameters are: $N = 20$, $n = 3$, $h_r : h_i = 1 : 3$, and $r = R/10$. In each figure, the FEM results obtained from COMSOL multiphysics simulations are also added for validating the TMM results.

two sets of results is observed for both the linear and the quadratic cases, so the accuracy of the TMM for the periodic SBH analyses is verified. Differences between the TMM and the FEM results are barely seen over the entire frequency range, despite some tiny discrepancy in Fig. 4(b) as the curves approach the maximum frequency.

Fig. 4 shows that the STL of the periodic acoustic duct increases over two frequency bands. For the linear case, the two frequency bands with high STLs are 230~920 Hz and 1000~1400 Hz. For the quadratic case, the two bands move downwards to 145~700 Hz and 765~1035 Hz, respectively. In Fig. 4, the first and second frequency bands are respectively highlighted by blue and yellow shades, which are referred to as the attenuation bands. For both cases, the first attenuation band exhibits a higher STL and a larger bandwidth compared with the second attenuation band, conducive to efficient low-frequency noise reduction. The detailed mechanisms that generate the two attenuation bands will be further explored in the later sections. It is obvious that the SBH profile has an overall impact on the STL curve. Changing the power-law profile from linear to quadratic will squeeze the attenuation bands toward the lower frequency side, amplify the STL peaks, and slightly compress the bandwidths.

3.1.2. Dispersive relation and bandgaps

To investigate the contributions from the periodicity, the band diagrams of the periodic duct embedded with either linear or quadratic SHBs are calculated and shown in Fig. 5. To start with, the real parts of the band diagrams are compared between the two configurations. Fig. 5(a) shows that two Bragg bandgaps are created over the same frequency ranges as the corresponding attenuation bands in Fig. 4(a). For the quadratic case, the agreement between the STL and bandgap variations is also observed, thus explaining the generation of the attenuation bands. The strength of sound attenuation provided by the proposed device can be understood from the imaginary part of the band diagram, which represents the intensity of attenuation that the incident sounds would undergo. As shown in Fig. 5(c) and (d), amplitudes of the imaginary parts become larger when switching from the linear profile to the quadratic profile, evidencing intensified attenuation.

Interestingly, the Bragg stopband frequency of the periodic duct embedded with either linear or quadratic SBHs is lower than that embedded with conventional insertions (sonic crystals) with the same lattice constant. Herein, we quantify the first bandgap by its starting frequency f_s, ending frequency f_e, center frequency $f_c = (f_s + f_e)/2$, and bandwidth $\Delta f = f_e - f_s$. Considering the lattice
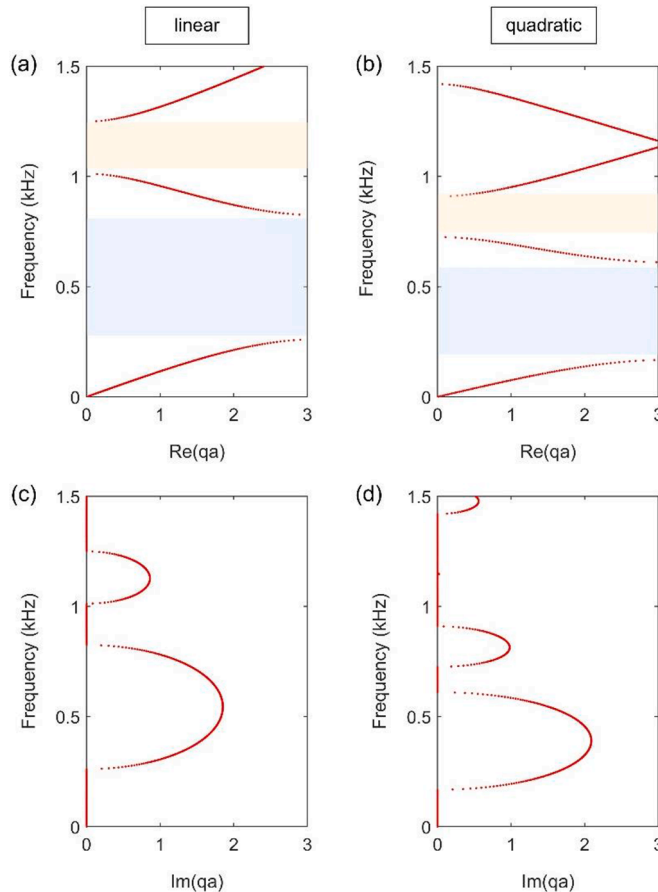
Fig. 5. Band diagrams of the acoustic duct with embedded periodic SBHs: (a) and (b) real parts; (c) and (d) imaginary parts for the linear and quadratic cases, respectively. Geometric parameters are: $N = 20$ and $r = R/10$. Bandgaps are identified by the blue and yellow shades in the real-part diagrams.

constant is $a = 4b = 0.2$ m, the normalized starting frequency $f_s a/c$ as observed in Fig. 5(a) is 0.152, the normalized end frequency $f_e a /c$ is 0.486, and the normalized center frequency $f_c a/c$ is 0.32. The relative bandwidth $\Delta f/f_c$ is 1.04. In Fig. 5(c), the normalized starting, ending and center frequencies for the first bandgap are 0.098, 0.359 and 0.23, respectively, and the relative bandwidth is 1.14. As Bragg stopband in conventional periodic structures typically occurs at $f_{Bragg} = c/2a$ (normalized frequency is 0.5), it is obvious that the proposed periodic SBH outperforms traditional sonic crystals in terms of low-frequency performance [33,34]. The reason why the Bragg stopband occurs at such low frequencies can be answered by the slow-sound effect of the SBHs. Since a sound speed reduction means that the propagating waves will take a longer time to pass through each unit cell, the unit cell length or the lattice constant becomes seemingly longer with respect to the wave slow-down. This effective slowing-down of sound speed c, or, in other words, equivalent elongation of the lattice constant a, drives down the operating frequency of the Bragg bandgap. Therefore, Bragg bandgaps of the periodic SBHs can start from a frequency that is lower than that determined by its periodic constant, which is also far lower than the cut-on frequency of the individual SBH unit.

To make a quantitative evaluation, we carried out a transient analysis on the acoustic wave propagation in the duct. The travelling wave is excited at the duct inlet by a sine pulse centered at 400 Hz, which coincides with the center frequency of the first attenuation band. The time-domain pressure signals, received at the four locations along the duct as depicted in Fig. 6(a) and (b), are calculated to understand the sound propagation process across each unit cell. As a comparison, the time histories in a regular duct without SBHs are shown in Fig. 6(a) and (c), and those of the periodic duct with SBHs are shown in Fig. 6(b) and (d). In both cases, a straight line is drawn to roughly show the time difference required for the pulse signal to pass through each unit cell. As the unit cell distances are kept identical, the slope of the straight line indicates the average speed at which the wave propagates. We can see that the line in Fig. 6(d) is more inclined compared with the line in Fig. 6(b), suggesting the wave is indeed slowed down by the periodic inclusions of SBHs, even at this relatively low frequency. Also the pressure signals for the regular duct without SBHs keep exactly the same waveforms, while for the duct with SBHs, the pressure signals are strongly attenuated as wave travels downwards. For the regular duct, the time required for the sound wave to travel through a periodic lattice is $\Delta t = 0.59$ms, which yields the sound speed in air as $a/(\Delta t) = 340$m /s. For the periodic duct with SBHs, the travel time is increased to $\Delta t = 1.2$ms, roughly doubles as compared to the regular duct. This means that the sound speed in the periodic SBHs is equivalently halved. Thus, the occurrence of Bragg stopband, as determined by $f_{Bragg} = c /2a$, appears two times earlier than regular Bragg reflections. This marks a significant advantage of using SBHs instead of conventional insertions to construct periodic structures for low-frequency noise control.
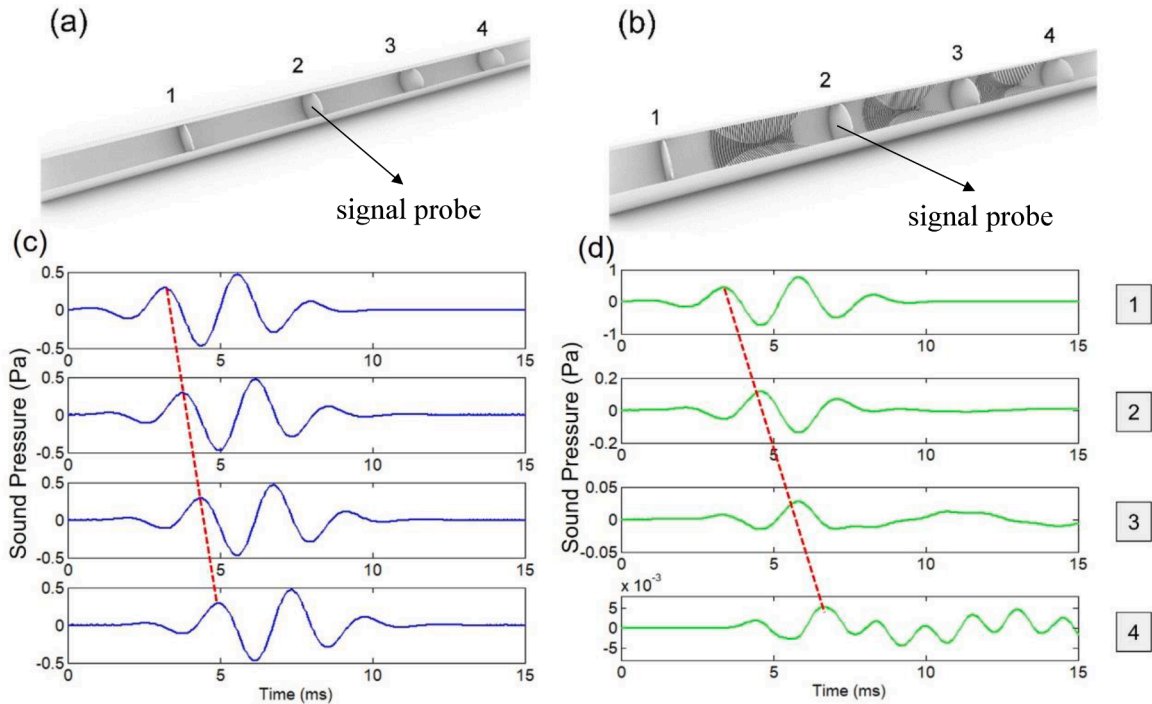
Fig. 6. Time histories of the sound wave travelling along a: (a) regular duct without SBHs; (b) periodic duct with embedded quadratic SBHs; (c) and (d) sound pressure signals received at the four defined locations. Geometric parameters of the periodic duct are: $N = 20$, $n = 3$, $h_r : h_i = 1 : 3$, and $r = R/10$. The regular duct has the same length and radius as the periodic duct. The incoming sound wave is tonal with frequency of 400 Hz, which coincides with the center frequency of the first bandgap.

3.2. Reflection and absorption coefficients

   To investigate the physical mechanisms behind the formation of those attenuation bands, the reflection and absorption coefficients of the periodic duct are calculated. The formulae for the calculation of different coefficients based on the TMM can be found in [27]. The results are shown in Fig. 7(a) for the linear case and Fig. 7(b) for the quadratic case. In both cases, the damping loss is first omitted to align with the previous discussions of FEM validation and bandgap calculation. Then a damping loss factor is introduced into the TMM formulation by complexifying the sound speed, i.e., $\tilde{c}_0 = c_0(1 + j\eta)$ where η is the assumed isotropic loss factor of air. $\eta = 0.05$ is first considered to show the effects with and without damping. Other structural parameters are the same as those used in Fig. 4.

   First, for the case without damping, Figs. 6(a) and (b) show that the reflection coefficient exhibits peak values close to one over two frequency ranges, in good agreement with those of the attenuation bands seen in Fig. 4, as well as the bandgap structures in Fig. 5. This correlation suggests that Bragg reflections, enhanced successively by the ensemble of unit cells, dominate the creation of the attenuation bands. As no damping is present in the duct, the absorption coefficient is constantly zero. After damping is introduced, it can be seen from Figs. 6(c) and (d) that the two coefficients have opposite overall tendencies as frequency increases. Although the first reflection peak attributed to Bragg reflections at low frequency is less affected, the second bandgap shows drastically different behavior responding to damping. At higher frequencies, the reflection coefficient diminishes, while the absorption coefficient rises. The contrast indicates that sound absorption, which is greatly improved due to the SBH effect, has become the dominant factor in the sound attenuation in the duct. To render a clear observation, the frequency ranges dominated by sound reflection are shaded in Fig. 7(a) and (b), while the arrows in Fig. 7(c) and (d) denote that the device enters into the frequency region which is more dominant by the SBH effect.
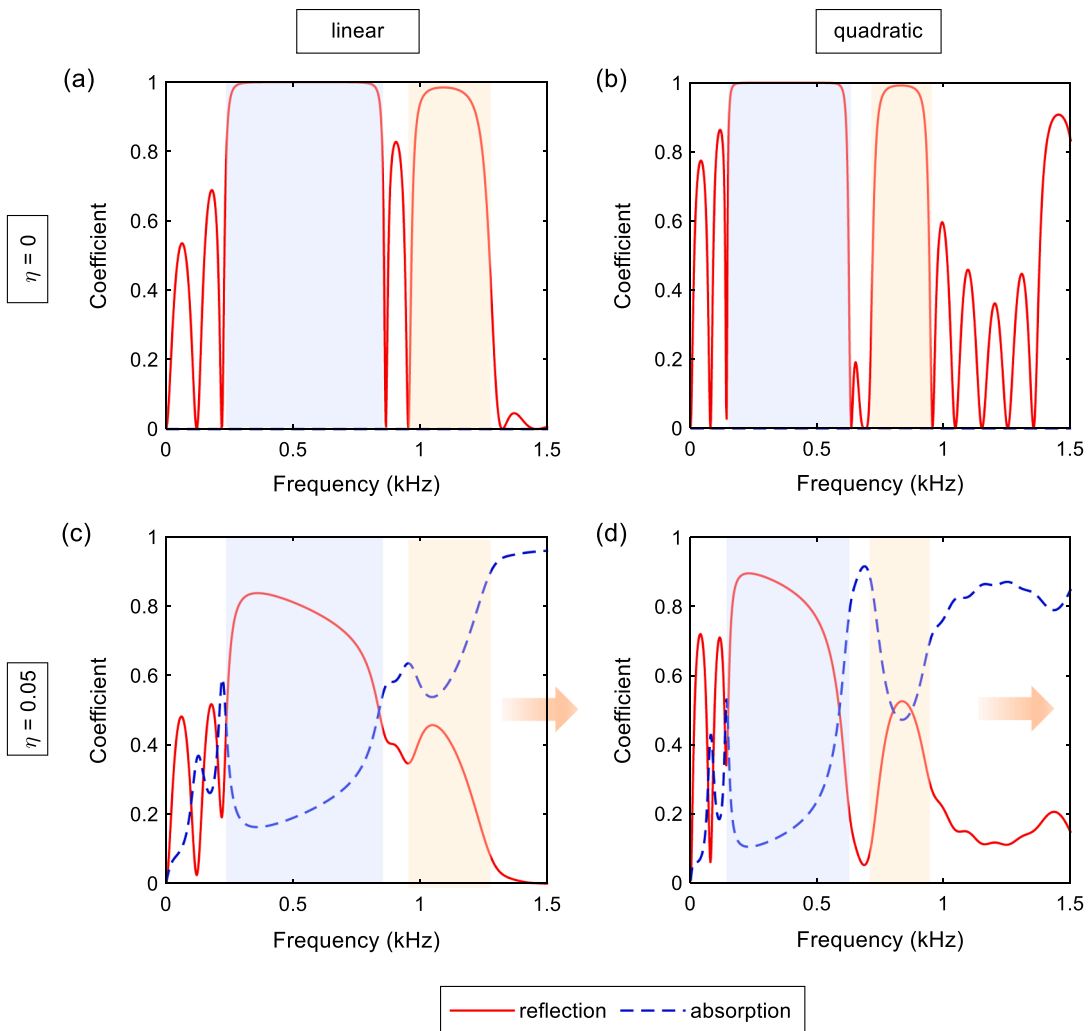
Fig. 7. Reflection and absorption coefficients of the acoustic duct with its SBHs following (a) linear profile, η=0; (b) quadratic profile, η=0; (c) linear profile, η=0.05; (d) quadratic profile, η=0.05. Other parameters are: $N = 20$, $n = 3$, $h_r : h_i = 1 : 3$, and $r = R/10$. The arrows in (c) and (d) denote that the device enters the frequency region which is more dominant by the SBH effect.

3.3. Results of parametric studies

3.3.1. Geometric parameters of the SBH

It has been shown in the above mechanism studies that inserting periodic SBHs into the acoustic duct brings benefits to sound attenuation, manifested by the low-frequency, high-STL attenuation bands. However, one question remains: whether these useful properties depend as much on the number of rigid rings as a classical SBH does. Previous work suggests that a sufficiently large number of rings need to be inserted into a SBH termination [24] in order to achieve appreciable SBH effects, which is challenging for real-world applications. To answer that question, the STLs of the acoustic duct with a varying number of rigid rings in each unit cell are calculated. Other geometrical parameters are kept as $n = 3$, $h_r : h_i = 1 : 3$ and $r = R/10$. The results of the linear and quadratic cases are plotted in Figs. 8(a) and (b), respectively, which clearly show that the attenuation bands are not sensitive to the number of rigid rings N. As N decreases from 40 to 10, no apparent deterioration of amplitude is seen in both plots and only a tiny shift at high frequency end is observed in the quadratic case. Fig. 8(a) demonstrates that a linear periodic duct with as few as 10 rings in each SBH can already entail a satisfactory performance. This relieves the harsh requirement on the number of rings suggested from previous single SBH study, which can be possibly attributed to the effect of periodicity. This also suggests that the formation of the attenuation bands must not only depend on the SBH effect, but also the periodicity. In Fig. 8(b), changes of the three STL curves are almost invisible over the first attenuation band and only become identifiable when the second attenuation band cuts on.

Fig. 8(c) and (d) show, for the linear and quadratic cases respectively, the STLs of the periodic duct with increasingly larger ratios between the ring thickness h_r and the cavity width h_i in every ring-wall-ring segment. As rings thicken and cavities diminish, the lumped admittance of each SBH unit will gradually deviate from the theoretical admittance that is required to realize the ideal SBH effects. In fact, the continuous admittance formula in [24] is derived by neglecting the thicknesses of the inner rings. Therefore, an
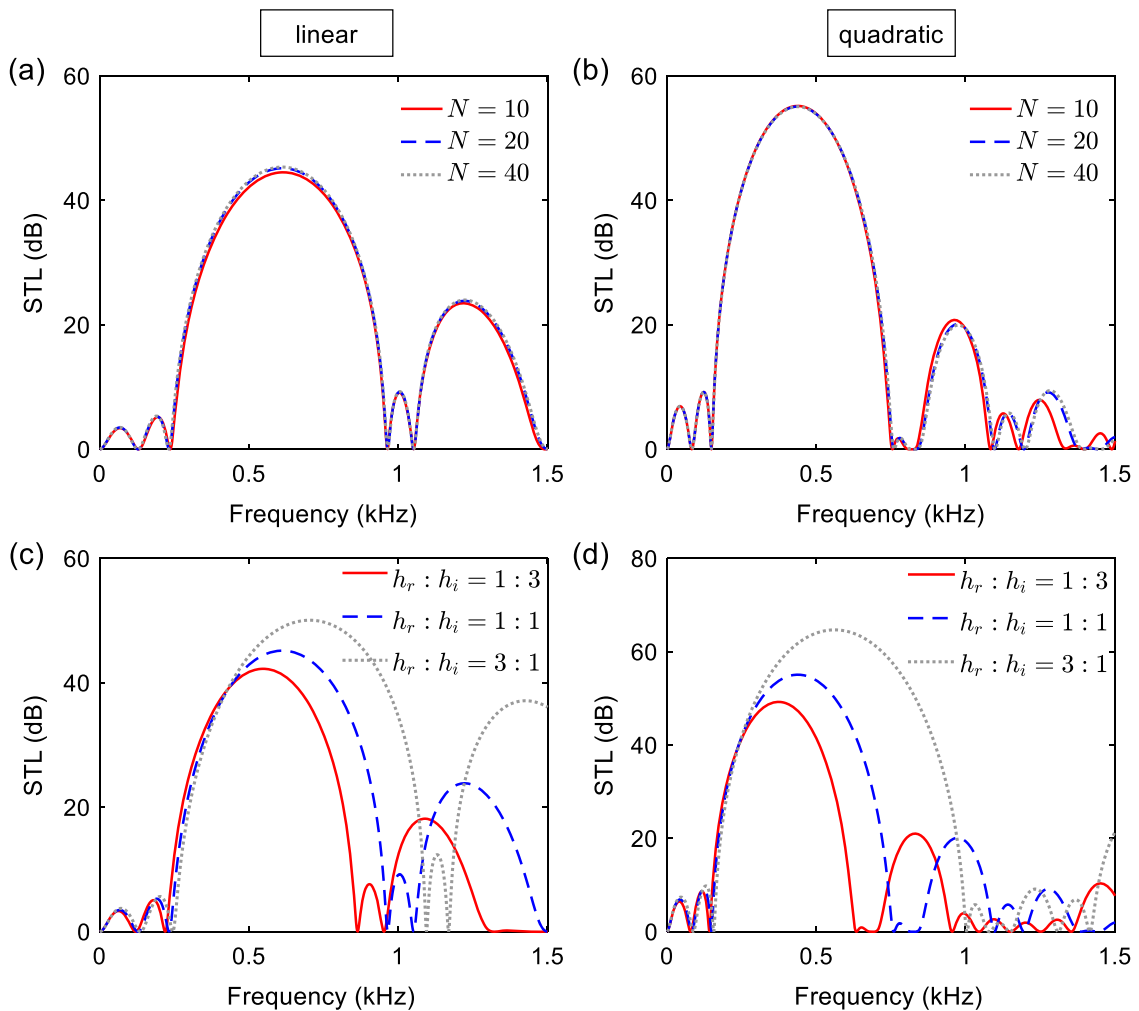
Fig. 8. STLs of the acoustic duct with growing (a)/ (b) number; (c)/ (d) thickness of rings in the SBH portion of each unit cell. For (a)/ (b), $h_r : h_i = 1 : 3$ and for (c)/ (d), $N = 20$. Other structural parameters are: $n = 3$ and $r = R/10$. (a)/ (c) are embedded with linear SBHs and (b)/ (d) are embedded with quadratic SBHs.

attenuation band of the periodic duct is expected to fade away if it is a result of the SBH effect. Surprisingly, this only happens to the second attenuation band in the quadratic case. For the two linear bands and the first quadratic band, the STL of the periodic duct becomes even stronger in terms of both amplitude and width. This contrast points to an underlying transition that the duct experiences as the frequency goes from low to high, which comes clearly earlier for the quadratic case. Over the vast frequency range that lies before that transition, substantial enhancements in the noise insulation of the duct can be obtained by simply tuning the thicknesses of the rings.

3.3.2. Periodicity

Let us examine the effect of periodicity on the sound attenuation. As shown in Fig. 9, the STL curve of the duct experiences a clear transformation as *n* increases from one to two, both for the linear and quadratic cases. The transformation is not limited to a positive alteration in the amplitude of the STL. Instead, we observe a more radical shift in the spectral composition of the results, signaling the emergence of the attenuation bands. Further adding unit cells onto the duct does not alter the overall trend of the STL curve, but the amplitudes in the attenuation bands continue to rise. We notice that this useful cumulative effect does not rely heavily on the number of unit cells – with only four SBH units, the calculated STL can reach as high as over 60 dB at 500 Hz for the linear duct and over 75 dB at 450 Hz for the quadratic duct. This is in drastic contrast to conventional acoustic metamaterials, which usually require a large group of unit cells to realize the desired function [36,38].

Differences between the attenuation intensities of the two bandgaps can be visualized further, by examining the distributions of sound pressure along the axis of the periodic duct. The sound pressure distributions shown in Fig. 10 are calculated based on the quadratic case with structural parameters: $N = 20$, $h_r : h_i = 1 : 3$ and $r = R/10$. Frequencies of Figs. 10(a) and (b) are selected respectively as 400 Hz and 1200 Hz, corresponding to the center frequencies of the bandgaps at which the duct acquires maximum intensities of attenuation. In both studies, the number of unit cells are gradually increased, so the competition between the SBH effect of each unit cell and the periodicity effect of the complete structure can be observed.

The amplification of sound pressure, a typical SBH characteristic, is observed in both figures over the middle part of the leading unit cell. This feature is better preserved by the second bandgap than by the first, with fluctuation of sound pressure in Fig. 9(b) being stronger than that in Fig. 10(a) over every subsequent unit cell. As a cost, the overall reduction of sound pressure is much slower for the second bandgap than for the first. In Fig. 10(a), the amplitude of sound pressure is significantly reduced after passing through the first unit cell and becomes barely noticeable in the third unit cell. Apparently, the same conclusion cannot be drawn from Fig. 10(b). This distinction between the two sets of results also hints at a simple explanation to the opposite behaviors of the second bandgap in Figs. 8 (c) and (d) – as the rings become thicker, that bandgap expands and amplifies in the linear case, while it shrinks and vanishes in the quadratic case – the maximum frequency is just not large enough for a linear SBH to take effect, so the whole spectrum of interest is still governed by the rule of periodicity. Moreover, because a quadratic SBH effect cuts on much earlier than its linear counterpart [24], it plays a dominating role in the formation of the second quadratic bandgap.

3.3.3. Influences of damping

It has been shown in Fig. 7 that damping significantly affects the reflection and absorption relationship of the periodic duct, especially at higher frequencies after the second bandgap. This indicates that a proper damping treatment could improve the STL performance. In this section, we further compare the STLs of the periodic duct with no, slight, and heavy damping treatments, where
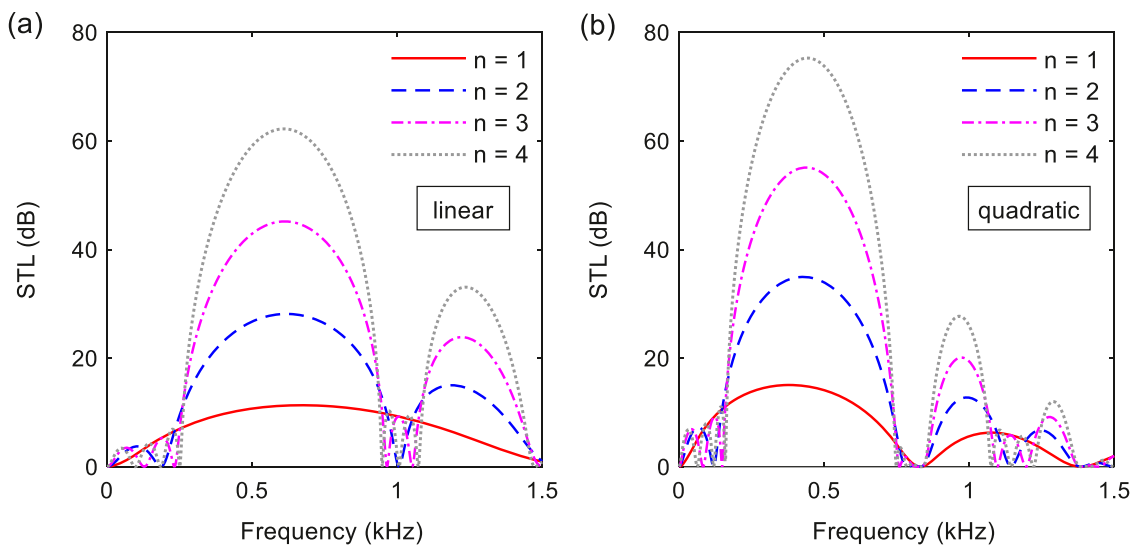
Fig. 9. STLs of the acoustic duct with a growing number of unit-cells, in which (a) linear; (b) quadratic SBHs are embedded. Other structural parameters are: $N = 20$, $h_r : h_i = 1 : 3$, and $r = R/10$.
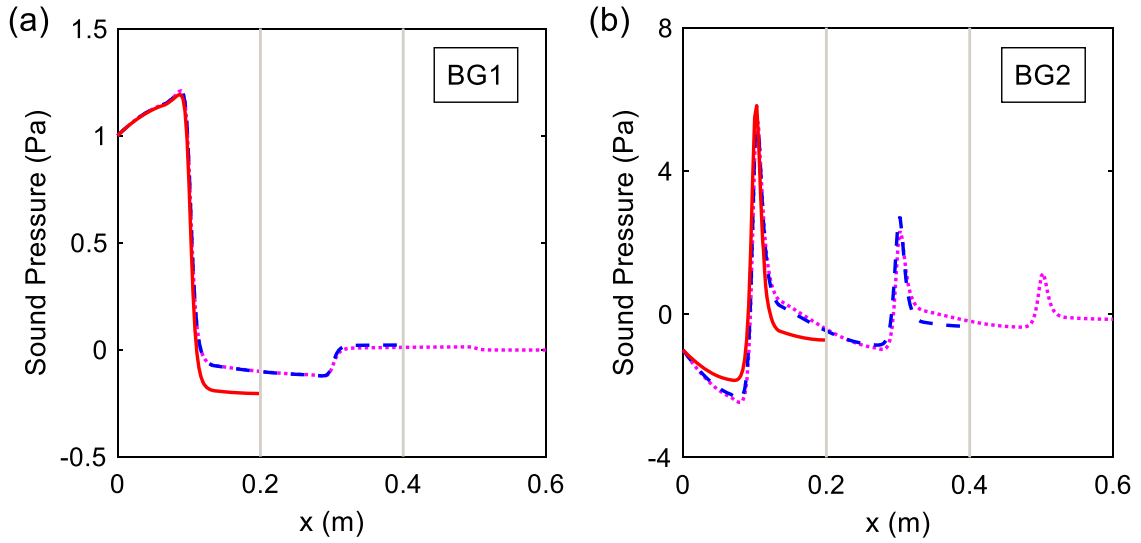
Fig. 10. Sound pressure distribution along the axis of the acoustic duct comprising one, two, and three unit-cells, with the frequency falling into the (a) first bandgap (400 Hz); (b) second bandgap (1200 Hz). Other structural parameters are: $N = 20$, $h_r : h_i = 1 : 3$ and $r = R/10$. The profile of radius in the SBH portion takes a quadratic form.

the damping loss factors η are taken as 0, 0.01, 0.05. Results of the linear and quadratic cases are respectively shown in Figs. 11(a) and (b), with structural parameters kept as $N = 20$, $n = 3$, $h_r : h_i = 1 : 3$ and $r = R/10$.

Compared with Fig. 4, Fig. 11 shows an obvious enhancement of the second attenuation band with increasing damping, and the enhancement is stronger in the quadratic case. Even with low damping, the quadratic case exhibits a systematic improvement in the STL over the second half of the spectrum. Raising η to 0.05 further elevates the STL curve, and almost eradicates the original STL valley between two attenuation bands. Note that similar improvements of STL, albeit smaller, also happen to the second attenuation band in the linear case. This suggests that, although the two attenuation bands are mainly governed by periodicity, the wave trapping effect of SBH still plays an indirect role in their formation, which is more visible when the SBH effect is amplified by the damping. The same statement can also be made to the first quadratic attenuation bands, where the damping-induced improvements, though marginal, are still recognizable. In summary, the formation of attenuation bands in the periodic duct is a product of the interplay between the Bragg scattering effect and the sonic black hole effect. When the frequency is low, that interplay is led by the Bragg scattering effect, which gives rise to the Bragg bandgaps as shown in Fig. 5; as the frequency increases, the SBH effect comes into play, which, with proper damping, leads to the enhanced noise insulation as shown in Fig. 11. The outcome of this useful interplay is a satisfactory overall sound insulation ability over a large portion of the considered frequency range.
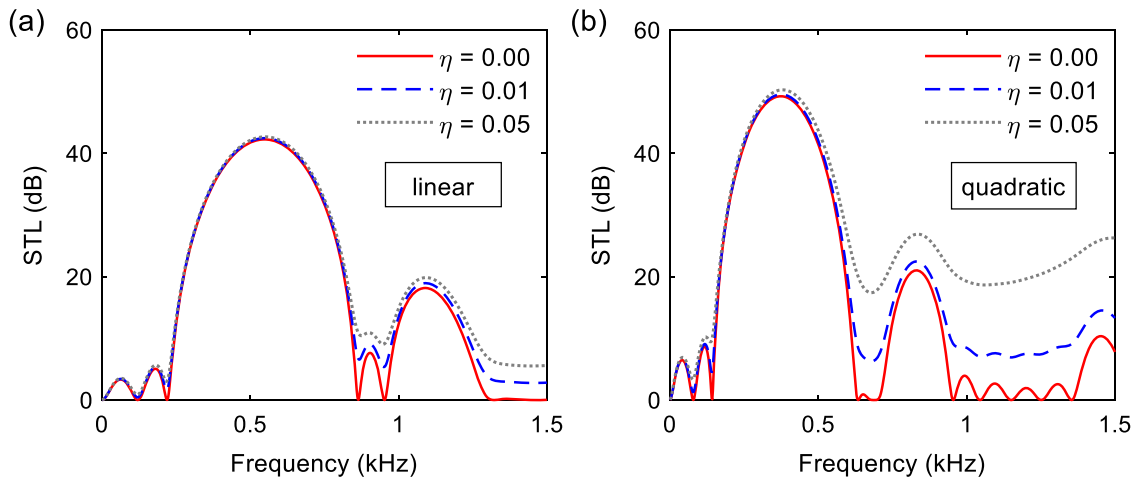
Fig. 11. STLs of the undamped ($\eta = 0$), slightly damped ($\eta = 0.01$), and heavily damped ($\eta = 0.05$) acoustic ducts, in which the SBH portion takes a (a) linear; (b) quadratic profile of radius. Damping is taken into consideration by assuming a complex sound speed $\tilde{c}_0 = c_0(1 + j\eta)$. Other structural parameters are: $N = 20$, $n = 3$, $h_r : h_i = 1 : 3$ and $r = R/10$.

3.3.4. Trade-off on SBH residual radius

Through the above discussions, the physical mechanisms for the improved sound insulation ability of the periodic duct have been revealed. However, one important and practically relevant question still remains, which concerns a trade-off on the residual radius of the SBH. While a small opening may facilitate sound insulation, it is not practical for engineering applications if the duct also needs to accommodate air passage with acceptable obstruction. To seek an answer, a parametric study is performed in which the residual radius r expands gradually from $R/10$ to $R/2$ while other structural parameters are kept as $N = 20$, $n = 3$, and $h_r : h_i = 1 : 3$. Fig. 12(a) shows the evolution of the imaginary part of the band diagram with the expansion of the residual. The STLs calculated at three parametric steps of $r = R/2$, $R/6$, and $R/10$ can be seen in Fig. 12(b) when $\eta = 0$ and in Fig. 12(c) when $\eta = 0.05$.

As expected, the results confirm that in the absence of damping, a small residual radius is a necessary requirement to achieve good sound insulation in the duct. As shown in Fig. 12(a), as the opening of each SBH unit becomes larger, the two bandgaps move upwards to higher frequencies with their attenuation intensities progressively being lowered. The second bandgap might even vanish when the residual opening is sufficiently large. This is also reflected in Fig. 12(b), in which the STL peak falls rapidly with the increase of r. Although the contradiction seems intractable, those results have actually shed a light on a desired trade-off between flow resistivity and sound insulation. The strategy lies in the fact that deteriorations of the bandgaps in Fig. 12(a) are not uniform throughout the parametric steps. The first few steps only see a minor drop of the attenuation intensity, and the drop only accelerates after $r = R/6$. Fig. 12(b) also indicates the reduction of STL from $r = R/10$ to $R/6$ is far more drastic than that from $r = R/6$ to $R/2$. From a practical point of view, the first attenuation band when $r = R/10$ is largely preserved when r is enlarged to $R/6$. The main disadvantage of $r = R/6$ is that sound insulation of the duct in the remaining frequency range is inadequate, but it can be conveniently ameliorated by further damping adjustment, which may requires the use of additional sound absorption materials inside the branch cavities. As shown in Fig. 12(c), with a loss factor of 0.05, the duct of $r = R/6$ exhibits a comparable performance with that of $r = R/10$ over the entire frequency range, but the former has an opening in the SBH that is nearly three times larger than that in the latter. In summary, a periodic duct with $r = R/6$ constitutes a good compromise between the competing requirements on flow and noise permeabilities.
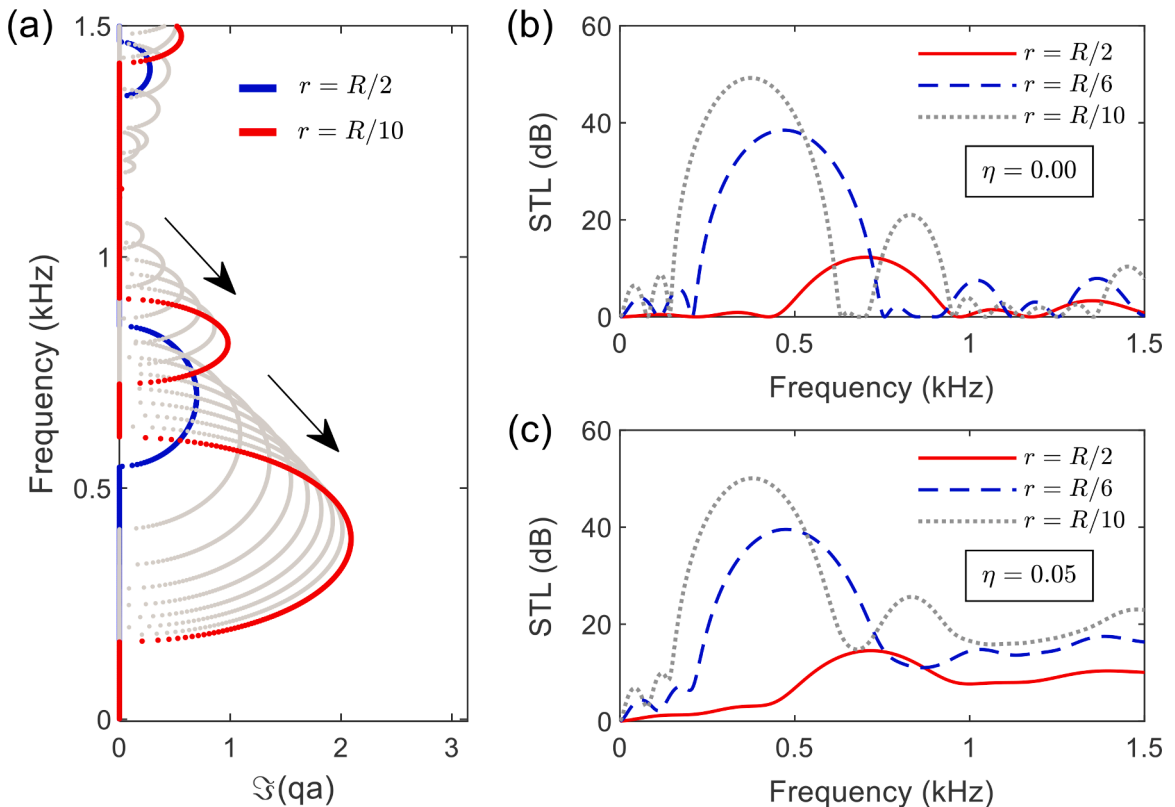
Fig. 12. Influences of the residual radius r on the noise reduction performance of the acoustic duct: (a) evolution of the imaginary-part band diagram when r narrows from $\boldsymbol{R}/2$ to $\boldsymbol{R}/10$; (b)/ (c) STLs of different residual radii when the duct is undamped ($\boldsymbol{\eta} = 0$) or heavily damped ($\boldsymbol{\eta} = 0.05$). Other structural parameters are: $N = 20$, $\boldsymbol{n} = 3$, and $\boldsymbol{h_r} : \boldsymbol{h_i} = 1 : 3$.

4. Experimental validation

4.1. Experimental set-up

To validate the results and the mechanisms discussed above, we fabricated a specimen through 3D printing (Original i3 MK3S+, UV curable resin) and measured its STL using the two-load method (ASTM E2611–09). The test-rig is shown in Fig. 13(a), which consists of an impedance tube (BSWA SW477), a power amplifier (BK 2706), and a data acquisition system (BBM PAK–MKII). The experiment was set up according to Fig. 13(c), with two microphones before the specimen and other two after. The STL is deteremined using the acoustic signals measured by the four microphones based on the four-microphone two-load method. The specimen comprises either one or three unit cells, each containing a quadratic SBH. The remaining geometric parameters are set as $N = 20$, $h_r : h_i = 1 : 3$ and $r = R/10$. Note that $R = 0.03$m equals the inner radius of the impedance tube. Although no sound absorbing material is inserted into the duct, the viscous and thermal loss caused by those narrow air cavities and apertures ($h_i = 1.5$mm) constitute a natural source of dissipation. An acoustic plane wave was generated by the loudspeaker installed at one end of the impedance tube. To produce two load cases, the other end of the impedance tube was set as either anechoic or rigid. The sound pressures were measured by four microphones (one pair mounted on the upstream tube and the other pair on the downstream tube) when the duct contains only one unit cell or a complete set of three unit cells. The sampling frequency is 8000 Hz. The STL can be obtained by processing the signals captured by the four microphones, the final result of which is taken as an average of five independent measurements.

4.2. Measurement results

The measured STL of the periodic duct is shown in Fig. 14(a), in which the simulated STL calculated by the TMM is also added for comparison. A good agreement between the two sets of results is observed in terms of the general trend, which validates the numerical simulation. The two attenuation bands can be easily identified from the experimental results, which proves the effectiveness of the proposed device. The discrepancies are mainly found in the amplitude of the second attenuation band, which can be attributed to the simplified estimation of damping. The actual damping in the system is too complicated to be simplified by an isotropic loss factor assigned to the complex sound speed, which might overestimate or underestimate the STL at certain frequencies. The discrepancies observed in Fig. 14 could also be attributed to the exclusion of the visco-themal effect in the model, which might be significant due to narrow gaps between SBH partitions.

In Fig. 14(b), the measured and simulated STL results with only one unit cell retained in the acoustic duct are presented. It can be seen that the two distinctive attenuation bands in the low-frequency disappear, which emphasizes the contribution from periodicity in the cascaded SBH unit cells. At higher frequencies above 1.5k Hz, the SBH effect also develops in a single unit cell, such that the STL
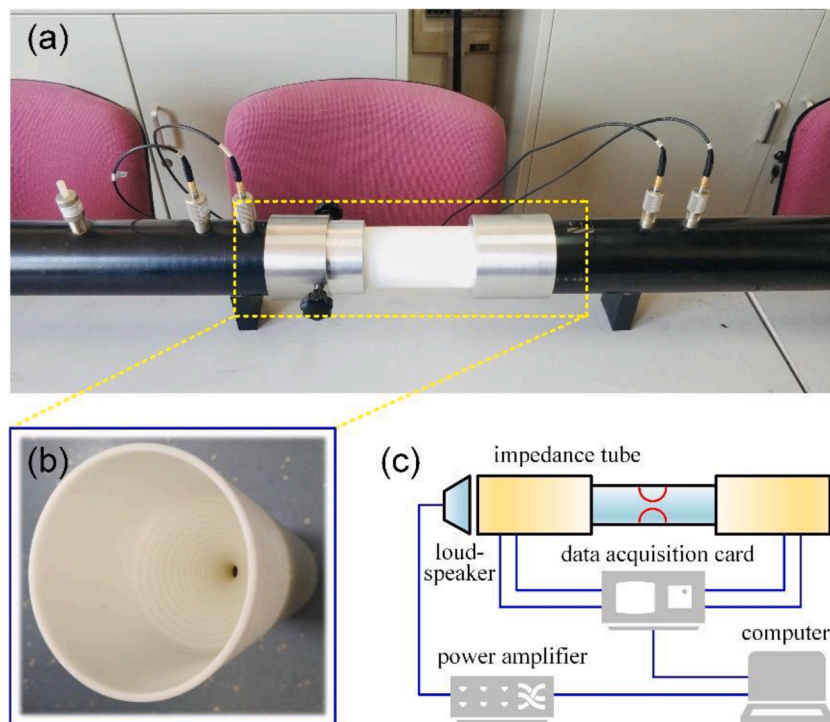
Fig. 13. STL measurement of the proposed acoustic device using an impedance tube: (a) photo of the measurement system; (b) close-up view of the 3D printed specimen; (c) schematic of the experimental set-up.
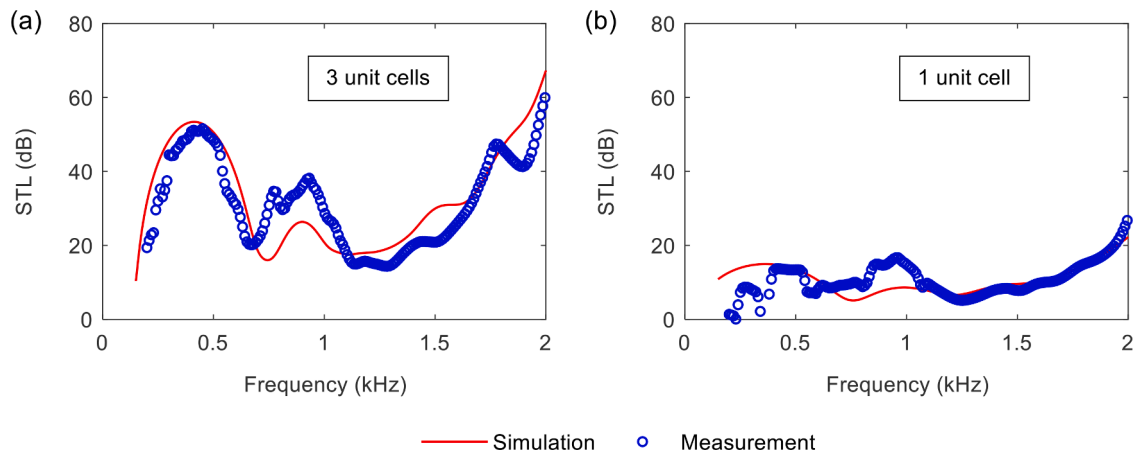
Fig. 14. Comparisons between the measured and simulated STLs of (a) the proposed periodic duct with three SBH unit cells; (b) only one unit-cell retained in the acoustic duct. The loss factor in the TMM is taken as $\eta = 0.05$.

curve continuously rises and the device can work fairly well for sound attenuation. In fact, most of the incident waves with frequencies higher than 1.5 kHz can be blocked by the very first unit cell, leaving the other two unit cells barely functional. As the improvement at relatively higher frequencies is not a result of periodicity, the omission of discussions on this topic in preceding sections is justified.

5. Conclusions

In this paper, the sound propagation and insulation in an acoustic duct with embedded periodic sonic black holes (SBH) are investigated. The SBH portion in each unit cell of the periodic duct is designed to have a symmetrical profile with either linear or quadratic variation of inner radii. A transfer matrix (TMM) model is built for the theoretical analyses, which is validated against finite element simulations. Based on the TMM model, the low-frequency sound propagation and insulation performance of the periodic duct has been thoroughly studied, via examining both band diagrams and sound transmission loss (STL) of a finite-length structure. The main conclusions are summarized as follows:

(1) The embodiment of periodic SBHs provides a feasible way for acoustic wave manipulation inside a duct device, and in particular an enhancement of its low-frequency sound insulation ability. Broad and strong attenuation bands are found in the STL of the periodic duct, which are steadily obtained by using as few as three unit cells. Compared with the conventional SBH with a closed termination, the proposed design relies less on the number of the rings but becomes more dependent on a small residual opening to effectively stop the incident waves. Thanks to the SBH-enabled energy focalization, a slight damping treatment could help achieve a trade-off between low flow resistivity and high sound insulation in the duct.
(2) The low-frequency and high-STL attenuation bands are enabled by a twofold physical mechanism: the Bragg scattering effect and the SBH effect. When the frequency is low where the damping-induced dissipation is weak, sound insulation in the periodic duct is mainly dominated by the Bragg scattering effect, manifested by the Bragg bandgaps emerging in the band diagram. The observed low frequency performance is attributed to an increase in the effective lattice constant as a result of SBH-induced sound speed reduction in the SBH cell. As the frequency increases, the SBH effect comes into play in a more pronounced manner, enabling the STL to rise again with the help of the inherent damping in the system. This transition happens earlier in the periodic duct with higher-order (quadratic) periodic SBHs compared with that with lower-order (linear) periodic SBHs.

CRediT authorship contribution statement

Yongzhen Mi: Conceptualization, Methodology, Software, Validation, Writing – review & editing. **Li Cheng:** Conceptualization, Writing – review & editing, Supervision, Funding acquisition. **Wei Zhai:** Conceptualization, Writing – review & editing, Funding acquisition. **Xiang Yu:** Conceptualization, Methodology, Software, Validation, Writing – review & editing, Funding acquisition.

Declaration of Competing Interest

The authors declare that they have no known competing financial interests or personal relationships that could have appeared to influence the work reported in this paper.

Acknowledgements

References

[1] M. Mironov, Propagation of a flexural wave in a plate whose thickness decreases smoothly to zero in a finite interval, Soviet Phys. Acoustics 34 (1988) 318–319.
[2] M. Mironov, V. Pislyakov, One-dimensional acoustic waves in retarding structures with propagation velocity tending to zero, Acoust. Phys. 48 (2002) 347–352.
[3] A.A. El Ouahabi, V.V. Krylov, D.J. O'Boy, Experimental investigation of the acoustic black hole for sound absorption in air, in: Proceedings of the 22nd International Congress on Sound and Vibration, Florence, Italy, 2015.
[4] N. Sharma, O. Umnova, A. Moorhouse, Low frequency sound absorption through a muffler with metamaterial lining, in: Proceedings of the 24th International Congress of Sound and Vibration, London, UK, 2017.
[5] C. Zhao, M.G. Prasad, F. Fisher, B. Rajavel, Performance of a modified double expansion chamber muffler inspired by Acoustic Black Hole theory, in: INTER-NOISE and NOISE-CON Congress and Conference Proceedings, NoiseCon20, New Orleans, USA, 2020.
[6] M. Mironov, V. Pislyakov, One-dimensional sonic black holes: exact analytical solution and experiments, J. Sound Vib. 473 (2020), 115223.
[7] N. Gao, B. Wang, K. Lu, H. Hou, Complex band structure and evanescent Bloch wave propagation of periodic nested acoustic black hole phononic structure, Appl. Acoustics 177 (2021), 107906.
[8] J. Deng, O. Guasch, L. Zheng, T. Song, Y. Cao, Semi-analytical model of an acoustic black hole piezoelectric bimorph cantilever for energy harvesting, J. Sound Vib. 494 (2021), 115790.
[9] Q. Fu, X. Du, J. Wu, J. Zhang, Dynamic property investigation of segmented acoustic black hole beam with different power-law thicknesses, Smart Mater. Struc. 30 (2021), 055001.
[10] V.V. Krylov, F.J.B.S. Tilman, Acoustic 'black holes' for flexural waves as effective vibration dampers, J. Sound Vib. 274 (2004) 605–619.
[11] N. Gao, Z. Wei, H. Hou, A.O. Krushynska, Design and experimental investigation of V-folded beams with acoustic black hole indentations, J. Acoust. Soc. Am. 145 (2019). EL79-EL83.
[12] H. Li, C. Touzé, A. Pelat, F. Gautier, X. Kong, A vibro-impact acoustic black hole for passive damping of flexural beam vibrations, J. Sound Vib. 450 (2019) 28–46.
[13] D.J. O'Boy, V.V. Krylov, V. Kralovic, Damping of flexural vibrations in rectangular plates using the acoustic black hole effect, J. Sound Vib. 329 (2010) 4672–4688.
[14] L. Zhao, F. Semperlotti, Embedded acoustic black holes for semi-passive broadband vibration attenuation in thin-walled structures, J. Sound Vib. 388 (2017) 42–52.
[15] W. Huang, H. Ji, J. Qiu, L. Cheng, Wave energy focalization in a plate with imperfect two-dimensional acoustic black hole indentation, J. Vib. Acoust. 138 (2016), 061004.
[16] H. Ji, X. Wang, J. Qiu, L. Cheng, Y. Wu, C. Zhang, Noise reduction inside a cavity coupled to a flexible plate with embedded 2-D acoustic black holes, J. Sound Vib. 455 (2019) 324–338.
[17] L. Tang, L. Cheng, Impaired sound radiation in plates with periodic tunneled Acoustic Black Holes, Mech. Syst. Signal Process. 135 (2020), 106410.
[18] L. Tang, L. Cheng, Ultrawide band gaps in beams with double-leaf acoustic black hole indentations, J. Acoust. Soc. Am. 142 (2017) 2802–2807.
[19] T. Zhou, L. Cheng, Planar swirl-shaped acoustic black hole absorbers for multi-directional vibration suppression, J. Sound Vib. 516 (2022), 116500.
[20] H. Li, C. Touzé, A. Pelat, F. Gautier, Combining nonlinear vibration absorbers and the Acoustic Black Hole for passive broadband flexural vibration mitigation, Int. J. Non Linear Mech. 129 (2021), 103558.
[21] M. Ouisse, D. Renault, P. Butaud, E. Sadoulet-Reboul, Damping control for improvement of acoustic black hole effect, J. Sound Vib. 454 (2019) 63–72.
[22] L. Ma, L. Cheng, Numerical and experimental benchmark solutions on vibration and sound radiation of an Acoustic Black Hole plate, Appl. Acoust. 163 (2020), 107223.
[23] A. Pelat, F. Gautier, S.C. Conlon, F. Semperlotti, The acoustic black hole: a review of theory and applications, J. Sound Vib. 476 (2020), 115316.
[24] O. Guasch, M. Arnela, P. Sánchez-Martín, Transfer matrices to characterize linear and quadratic acoustic black holes in duct terminations, J. Sound Vib. 395 (2017) 65–79.
[25] O. Guasch, P. Sánchez-Martín, D. Ghilardi, Application of the transfer matrix approximation for wave propagation in a metafluid representing an acoustic black hole duct termination, Appl. Math Model 77 (2020) 1881–1893.
[26] J.P. Hollkamp, F. Semperlotti, Application of fractional order operators to the simulation of ducts with acoustic black hole terminations, J. Sound Vib. 465 (2020), 115035.
[27] Y. Mi, W. Zhai, L. Cheng, C. Xi, X. Yu, Wave trapping by acoustic black hole: simultaneous reduction of sound reflection and transmission, Appl. Phys. Lett. 118 (2021), 114101.
[28] X. Zhang, L. Cheng, Broadband and low frequency sound absorption by sonic black holes with micro-perforated boundaries, J. Sound Vib. 512 (2021), 116401.
[29] L. Tang, L. Cheng, Broadband locally resonant band gaps in periodic beam structures with embedded acoustic black holes, J. Appl. Phys. 121 (2017), 194901.
[30] C.A. McCormick, M.R. Shepherd, Design optimization and performance comparison of three styles of one-dimensional acoustic black hole vibration absorbers, J. Sound Vib. 470 (2020), 115164.
[31] T. Zhou, J.D. Chazot, E. Perrey-Debain, L. Cheng, Partition of unity finite element method for the modelling of acoustic black hole wedges, J. Sound Vib. 475 (2020), 115266.
[32] L. Tang, L. Cheng, Characterization of acoustic black hole effect using a one-dimensional fully-coupled and wavelet-decomposed semi-analytical model, J. Sound Vib. 374 (2016) 172–184.
[33] J. Leng, V. Romero-García, A. Pelat, R. Picó, J.-.P. Groby, F. Gautier, Interpretation of the acoustic black hole effect based on the concept of critical coupling, J. Sound Vib. 471 (2020), 115199.
[34] X. Yu, Z. Lu, L. Cheng, F. Cui, On the sound insulation of acoustic metasurface using a sub-structuring approach, J. Sound Vib. 401 (2017) 190–203.
[35] R. Ghaffarivardavagh, J. Nikolajczyk, S. Anderson, X. Zhang, Ultra-open acoustic metamaterial silencer based on Fano-like interference, Phys. Rev. B 99 (2019), 024302.
[36] D.Y. Kim, J.G. Ih, Wideband reduction of in-duct noise using acoustic metamaterial with serially connected resonators made with MPP and cavities, Appl. Phys. Lett. 116 (2020), 251904.
[37] M. Sun, X. Fang, D. Mao, X. Wang, Y. Li, Broadband acoustic ventilation barriers, Phys. Rev. Appl. 13 (2020), 044028.
[38] Y. Mi, Z. Lu, X. Yu, Acoustic inerter: ultra-low frequency sound attenuation in a duct, J. Acoust. Soc. Am. 148 (2020). EL27-EL32.
[39] X. Yu, Z. Lu, T. Liu, L. Cheng, J. Zhu, F. Cui, Sound transmission through a periodic acoustic metamaterial grating, J. Sound Vib. 449 (2019) 140–156.